A 4D Soil-Structure Interaction Model Testing Apparatus

Riccio, Thomas; Romero, Tomas; Previtali, Marco; Mánica, Miguel; Ciantia, Matteo

Published in:
Geotechnical Testing Journal

DOI:
10.1520/GTJ20230581

Publication date:
2024

Document Version
Peer reviewed version

This is an article accepted for publication in Geotechnical Testing Journal, Copyright @ 2024, ASTM International, West Conshohocken, PA, DOI: 10.1520/GTJ20230581

A 4D soil-structure interaction model testing apparatus

Thomas Riccio[1)], Tomas Romero[2)], Marco Previtali[1)], Miguel Manica[2)], Matteo Ciantia[1*,3)]

[1)] School of Science and Engineering, University of Dundee

[2)] Institute of Engineering, National Autonomous University of Mexico, Mexico

[3)] Department of Earth and Environmental Sciences, University of Milano Bicocca

* Corresponding author (m.o.ciantia@dundee.ac.uk)

Abstract

A new three-axis loading frame has been developed to enable real-time visualisation of in situ soil and rock structure interactions via X-ray tomography during small-scale model testing. The constructed frame is capable of performing a wide range of small-scale $1g$ tests and can accommodate monotonic and cyclic actuation under both load and displacement control. The compact size of the system enables remote multi-axis operation from within an X-ray cone-beam scanning bay, a capability which is owed to a comprehensive design process. Design and fabrication involved a blend of physical and numerical experiments to assess suitable construction materials and performance. In this scope, the new equipment is discussed and its capability is showcased.

Keywords: loading frame, physical testing, pile installation, soil-structure interaction, X-ray computed tomography

Nomenclature

$+F$	Tensile applied force
$-F$	Compressive applied force
ϕ	Chamber diameter
σ_c	Rock unconfined yield stress
θ	Rotation angle
θ_{peak}	Peak rotation angle
a	Residual displacement
D	Pile outer diameter
D_s	Specimen diameter
E_a	Aluminium stiffness
E_n	Nylon stiffness
E_p	Pile stiffness
E_s	Sample material stiffness

F	Applied force
f	Cyclic frequency
F_p	Force exceeding F_{max}
F_{cyc}	Cyclic applied force
f_l	Linear pile deflection component
F_{max}	Maximum compliance force
f_{Nl}	Non-linear pile deflection component
$F_{z,peak}$	Maximum cycle peak load
g	Gravity
H_v	Sample heave volume
I	Second moment of area
k	System stiffness
K_l	Frame load stiffness
K_R	Pile relative stiffness
K_{ref}	General frame stiffness
K_{ul}	Frame unload stiffness
L	Pile length
L/D	Pile slenderness ratio
L_p	Pile plug material height
L_z	Total pile penetration
M	Beam moment
M_L	Peak moment
p	Soil resistance
P_u	Lateral load at 0.1D
P_v	Approximate pile volume
P_z	Plug position
Q_o	Overall frame capacity
Q_{wo}	Overall frame capacity without nylon components
R_d	Relative density
t_w	Wall thickness
u	Displacement (+) or (-) associated with loading direction or state
u_{cyc}	Cyclic displacement amplitude
V	Beam shear

x	x direction (single motor horizontal direction)
y	y direction (dual motor horizontal direction) or pile defection
z	z direction (quad motor vertical direction)
AGL	Above ground level
BGL	Below ground level
FOS	Factor of safety
GL	Ground level
SD	Standard deviation

1 Introduction

In geotechnics, small scale physical testing plays a major role in understanding soil and rock-structure interactions (Wood, 2004), typically facilitated by in-house developed devices. Previous examples of small-scale testing devices include those by Peng et al. (2006); Arshad & O'Kelly (2014) and LeBlanc et al. (2010), which have been used to study the long-term cyclic loading behaviour of scaled pile foundations. Other apparatus have been developed too, including large model boxes and bespoke apparatus specifically for studying the displacement of model pipeline ploughs (Robinson et al., 2019) or screw pile performance (Davidson et al., 2022), tubular steel containers to study shallow footing settlements in soft rock (Castellanza et al., 2009; Ciantia et al., 2018), and half circular/plane strain chambers to study in-situ soil-pile (White & Bolton, 2004) and Cone penetration test (Arshad et al., 2014) installation behaviour. Additional examples include miniature triaxial (Cheng et al., 2020) and axial pile-testing apparatus (Doreau-Malioche et al., 2018; Alvarez-Borges et al., 2022b), those which were specifically developed to be used within an X-ray computed Tomography (XCT) bay.

X-ray tomography is recognised as a useful tool in geotechnics to study in-situ behaviour as it can distinguish variations in material density and internal structure (Phillips & Lannutti, 1997; Alvarez-Borges et al., 2022b) that are not typically revealed by conventional instrumentation. The microresolution of XCT can therefore be used to observe material kinetics like particle rotation (Cheng et al., 2020), grain crushing (Karatza et al., 2019), and porosity changes (Alvarez-Borges et al., 2022a) that may be realised through imaging analysis techniques like digital image/volume correlation (Tudisco et al., 2017; Doreau-Malioche et al., 2018). These observations can thereafter aid in the process of numerical model validation for methods such as the discrete element method (Doreau-Malioche et al., 2018; Cerfontaine et al., 2023) or the continuum-based particle finite element (FE) method (Previtali et al., 2023; Oliynyk et al., 2021; Ciantia et al., 2024; Monforte et al., 2022). Various researchers, including some of those mentioned above, have used XCT as a technique to study, quasistatically or continuously, the micro- and macro-scale behaviour of soils. Some examples include incremental scans performed on element tests such as triaxial (Desrues et al., 2018; Cheng et al., 2020; Cnudde & Boone, 2013) or direct shear (Bull et al., 2020), shear tests, observations of plant growth and soil penetration (Viggiani et al., 2015) and lateral/axial pile behaviour (Otani et al., 2006; Sato et al., 2018; Alvarez-Borges et al., 2022a), and earlier pile studies in calcareous materials (McCarel & Beard, 1984; Murff, 1987). More recently, four-dimensional (4D) approaches (i.e., three-dimensional [3D] plus time resolution (Ferreira et al., 2022)) have become of interest (e.g., Larsson et al. (2023); Alvarez-Borges et al. (2022b)) and which can overcome some challenges of traditional static/quasistatic approaches. This

becomes particularly advantageous in studies where pauses, sample disturbances, or changes in the stress state may influence the prevailing behaviour of an otherwise continuous test. The benefits of both small-scale testing and in-situ observations are therefore apparent. Achieving this integration is challenging, particularly in cases of nonstatic testing (i.e., 4D time-resolved testing) or when dealing with multidirectional loading for which there are few examples in the literature (e.g., Mayoral et al. (2016) and Su (2012)).

Within this context, the article presents the development of a new multi-axis loading frame, operable from within an XCT bay and capable of 4D testing. The discussion covers design considerations, including material and instrumentation selection, all while maintaining a budget of approximately £15,000 (USD 19,000). Some critical aspects are also described, including the development of the control system and its performance, as well as the systems' compliance under loading, which is crucial for accurate local displacement measurement. System performance is demonstrated through a small scale open-ended (OE) pile installation and lateral loading test performed in Congleton silica sand (HST-95) sand, complemented by time-resolved radiography, offering insights into in-situ behaviour during testing, a perspective not captured by static incremental scanning. Other complementary examples are also presented, including the behaviour of tree-roots during push-over, after Zhang et al. (2020a,b) and Liang (2015), and the vertical cyclic performance of a small-scale OE pile installed in soft low-medium density chalk, revealed by 3D XCT scans performed at different stages of testing.

2 Multi-axis system

The multi-axis frame, shown in Figure 1, was designed to fulfil geometrical, weight and operational constraints. Size and weight were dictated by the University of Dundee's SMART lab CT scanner, which comprises a 225 kWh X-ray cone-beam scanner stationed inside a bay of a height and width of 1110 mm and 2130 mm, respectively, and with a weight limit of 50 kg.

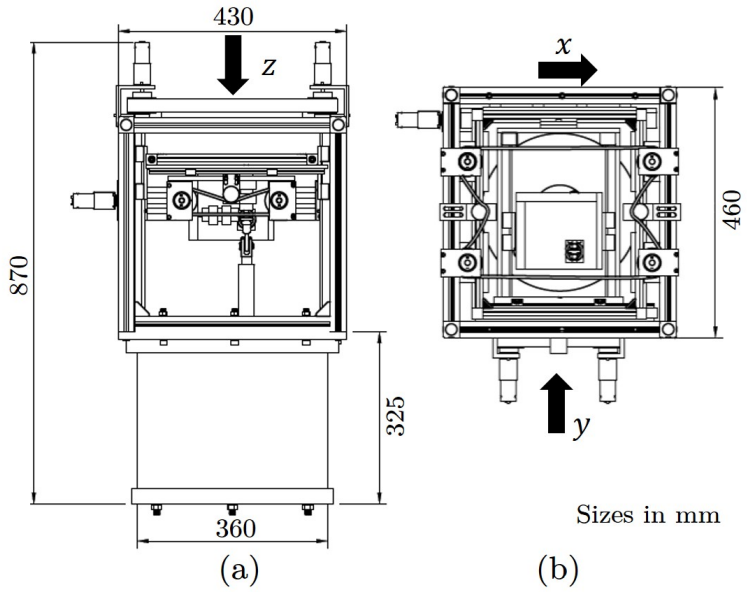

Figure 1: The final design of the multi-axis loading frame in large chamber mode: (a) front view and (b) plan view. Note x, y, and z are the actuation directions

The operational constraints of the frame were based upon the goal of installing small-scale piles (diameter $D < 20$ mm) into various soft rock materials (i.e., unconfined compressive strength of $\sigma_c < 4$ MPa), enabling the study of critical rock-structure interaction as part of the EPSRC project: Installation and Cyclic Loading Effect on Piles installed in Chalk (ICE-PICK: EP/W00013X/1). Based on prior physical (Alvarez-Borges et al., 2022a; Riccio et al., 2023) and numerical studies (Zheng et al., 2023), a vertical (z) and horizontal (x and y) load application of 5 kN and 500 N, respectively, were prescribed.

2.1 Material selection and hardware

To achieve a low relative weight, off-shelf Bosch Rexroth mechanic elements (Bosch Rexroth, 2023) were used to fabricate the main outer and inner frame components, shown in 2 (part ii, viii). On the other hand, the inner box (see Figure 2, part vii) and the frames' top/base plate (see Figure 3, part iii/viii) were machined from 6061 aluminium to achieve sufficient strength rigidity. .

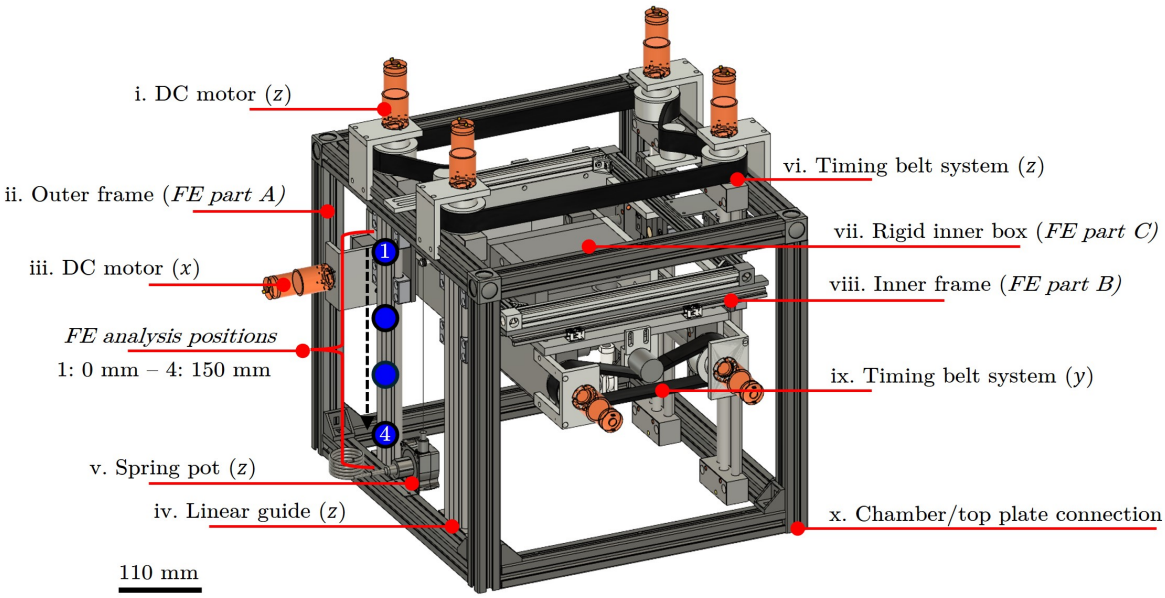

Figure 2: Multi-axis frame actuator and primary components detailed from i to ix. Also, showing frame actuator height positions for finite element analysis, see dark markers and italic text

Actuation was facilitated by linear motion IGUS Drylin SLW guides with inner Iglidur bearings (IGUS, 2023) assembled on the vertical and horizontal loading axes (see Figure 2, part iv). The vertical axis was driven by 4No. 1:264 MFA DC motors (see Figure 2, part i) capable of producing 4.1 N-m at 12 v (MFA Motors, 2023) while a timing system using Brecoflex 25AT10 steel-reinforced polymer belts (Breco-flex, 2023) maintained synchronicity of the linear guides (see Figure 2, part vi). A similar system was used for the y direction but with approximately 50 % of the vertical torque (see Figure 2, part ix). The x direction was driven via 1No. 1:516 low noise MFA DC motor (MFA Motors, 2023) (1.18 N-m at 12 v, see Figure 2, part iii). Each axis was configured on cascading linear guides as shown in Figure 1b and 2. Therefore, they were independently operable, enabling multi-directional testing coupled at the structure within the rigid box (see Figure 2 part vii and Figure 4).

3No. OMEGA (OMEGA, 2023) miniature load cells, capable of measuring 5-kN compressive or tensile load (accuracy: ± 0.20 %), were connected to a rod end assembly inside the rigid box, as shown later in Figure 4. This connection registered load readings in the x, y, and z directions and allowed for purely vertical, lateral free-head,

and fixed-head loading. Displacement measurement for each axis was obtained via 3No. TE connectivity SP1 linear spring pot displacement sensors (accuracy: ± 0.25 %) (TE Connectivity, 2023), see Figure 2, part v).

The base plate of the frame actuator was developed to accommodate both small and large chamber assemblies, which are shown in Figure 3a and 3b, respectively. The chambers were fabricated from Perspex with an E ≈ 3 GPa and $\nu \approx 0.370$. The small chamber (sized 280 mm by ϕ 130 mm and with a 5-mm wall thickness (t_w)) comprised a compression plate that restrained the tube in the centre of the frame's base and top plate. During radiography or lab floor tests, this was supported by aluminium columns (see Figure 3a) or when in-test CT scanning was conducted, hollow aluminium tubular sections were utilised. The latter with the goal of reducing X-ray imaging artefacts generated by significant disruption to the X-ray path, such as star, streak, and other artefacts like beam hardening (Smith & Augarde, 2015). These otherwise make quantitative (e.g., density mapping) and qualitative (visual observations) more challenging. The large chamber (sized 280 mm by ϕ 360 mm and $t_w = 30$ mm) (see Figure 3b) was fixed to the frame using the base and top plate via the 12No. M10 studs that were resin-anchored and tapped in place, whose capacity was validated through ancillary tension tests. The different chamber sizes helped to facilitate high-quality CT scanning (i.e., the smaller chamber allowed for a higher image resolution).

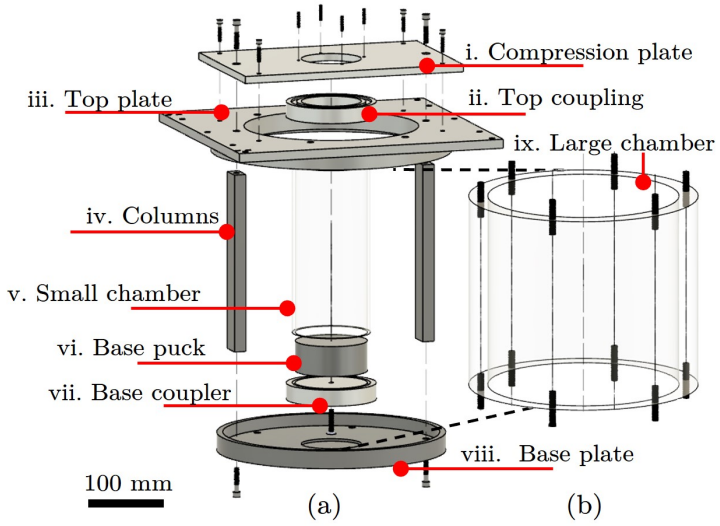

Figure 3: Chamber assemblies for the multi-axis system. (a) The ϕ 130-mm small chamber arrangement with aluminium columns (replaceable with hollow aluminium tubular sections) and (b) the ϕ 360-mm large chamber assembly

2.2 Design optimisation and numerical analysis

Prior to fabrication of the final design, FE numerical analyses were performed to verify the frame's capability. Emphasis was placed on the soundness of the outer frame by simulating different configurations of the system using the FE module in Fusion 360 (Autodesk, 2023). The equipment was separated into three main parts: (a) the outer frame, (b) the inner frame, and (c) the rigid reaction box, as shown previously in Figure 2, part ii, vii, and viii. Analyses were performed assuming a linear elastic behaviour of materials, and as the equipment was predominately planned to be manufactured from aluminium (T6061 anodised $E_a = 70$ GPa), load capacity was determined in accordance with the ADM-2015 design guidance (The Aluminium Association, 2015). This prescribed a safety factor of 1.65 for both tensile and compressive yield limits. Lower stiffness elements, such as

the linear Iglidur nylon bearing guides (E_n = 2.4 GPa) (IGUS, 2023), were also taken into consideration when performing the numerical analysis and were assumed to uphold the same criteria as the aluminium components.

Simulations were performed assuming four different vertical positions of the inner frame (in vertical increments of 50 mm), as shown in Figure 2a, covering the vertical displacement range of approximately 150 mm. All displacement components were constrained on the contact surface between the base plate of the frame and the Perspex chamber, and the load was applied on the sliding plates of the linear motion rails, where the inner frame was connected (see Figure 2a). The maximum overall load capacity (Q_o) for all directions was achieved in the lowest position of the inner frame (see Figure 2a), where the base plate contributed to the rigidity of the system as summarised in Table 1. The average Q_o in the z direction was approximately 5.68 kN, limited only by the nylon lead screw connectors of the linear guides. The average Q_o for the x and y direction was 1.54 kN and 5.72 kN, respectively, although were, in both directions, limited by the rod end connection that had a lower capacity of approximately 500 N. When ignoring the sliding plates of the linear motion rails, the average frame capacity (Q_{wo}) was between 1 and 5 times greater in all directions (see Table 1), indicating that the nylon components could be changed to increase system capacity.

Table 1: Ultimate load conditions at FOS=1.65 for multi-axis system determined from FE analyses

System	Position (mm)	x	y	z
Overall system (kN) (Q_o)	0	1.25	3.64	4.65
	50	1.30	3.50	4.93
	100	1.64	7.42	5.47
	150	1.97	8.34	7.67
Without nylon (kN) (Q_{wo})	0	3.74	7.71	21.47
	50	4.26	9.10	30.12
	100	4.12	9.98	32.64
	150	4.59	11.41	29.51
Q_{wo}/Q_o	**Avg.**	**2.81**	**1.67**	**5.00**

3 Frame compliance

Compliance issues are caused by mechanical components in a system having some degree of deformation. In the case of no local measurement, this can result in underestimation of geomaterial stiffness, as the measured displacement is based on a series spring of system (K) and sample stiffness (E_s). Depending on K and E_s, local sensors may be required to obtain accurate displacement (Perbawa et al., 2019). Alternatively, global displacement may be corrected to account for this spring, removing system deformation. To quantify system compliance, and to correct test results, the frame was arranged with a locally instrumented rigid sample ($E_s \approx 200$ GPa) (see Figure 4) which was subjected to a series of load cycles, in each direction.

All tests were performed at a displacement-controlled rate of 0.03 mm/s and local displacement sensors attached on part i and ii (see Figure 4) were used to correct any unrelated compliance associated with the set up. The deformation characteristics observed were simplified to linear spring models and used to rectify global displacement data. Note the following conventions are used: F is applied force, K is system stiffness, and u is measured

displacement. Subscripts x, y, and z describe direction, whereas compressive and tensile loads are - and +, respectively. In the x direction, $F_{x,+}$ is associated with $u_{x,-}$ and for the y direction $F_{y,+}$ is associated with $u_{y,+}$. Load and unload stiffnesses are described by K_{ul} and K_l, (for each + and - load case), or $K_{+,-}$ where a single stiffness is suitable to describe the full system.

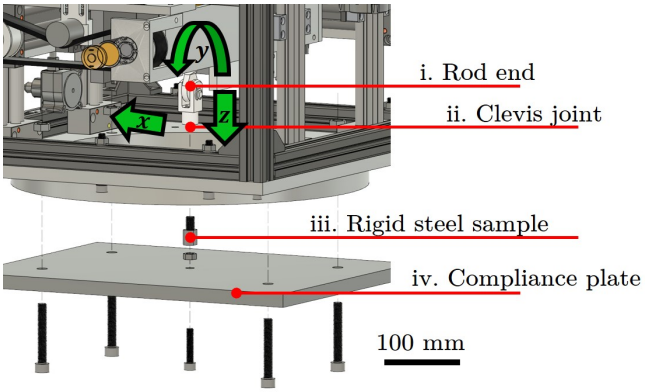

Figure 4: Compliance testing assembly for the multi-axis frame and key components (i-iv)

3.1 Numerical FE simulation of vertical frame deformation

Numerical FE simulations were also performed to realise critical deformation zones of the system, verify the measured deformation, as well as compare idealised model conditions to those of the built frame. An elastic model was considered (as before) and so the validity of superimposition of effects was thought reasonable. This simplified the analysis and eased the challenge associated with node limitations in the Fusion 360 academic license. The model was divided into two parts, namely the reaction box and the inner and outer frames (see Figure 5).

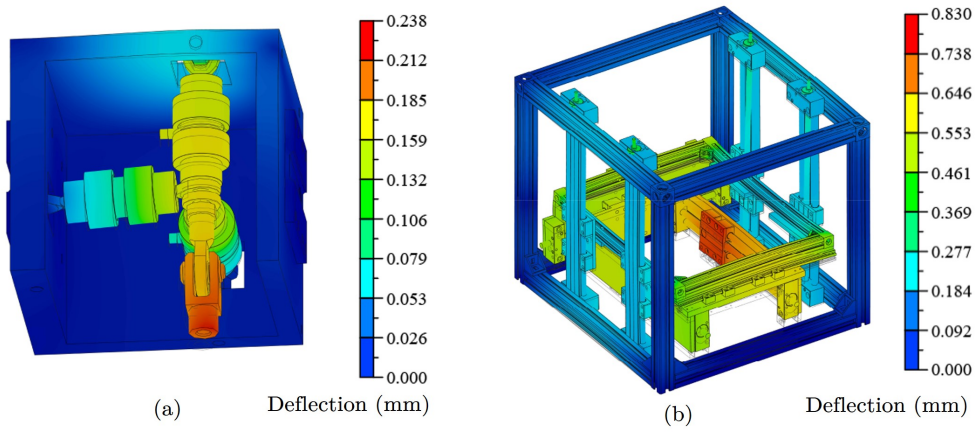

Figure 5: FE model contours of vertical displacements in millimetres of (a) the rigid box and (b) the outer and inner frames

When modelling the reaction box (see Figure 5a), displacements were restrained at the connection with the horizontal linear motion system of the inner frame, and the vertical load ($F_{z,-} = 3500$ N) was applied directly at the rod end connection, mimicking the compliance set up (see Figure 4). The reactions obtained were then applied to the model of the outer and inner frames (see Figure 2) at the connecting plates with the rigid box in the horizontal linear motion system (see Figure 5b). Figure 5 shows the resulting contours of vertical displacement,

where maximum values of $u_{z,a} = 0.24$ mm and $u_{z,b} = 0.83$ mm were obtained in the rigid box and the outer and inner frames, respectively. Therefore, a total vertical displacement of $u_{z,a+b} = 1.14$ mm. Predicting the real apparatus compliance was difficult and, as shown in the following section, the numerical simulation underestimated the actual system deformation. Nevertheless, the assessment was valuable for definition of the final frame configuration and to identify areas in the system susceptible to deformation (namely, the rod-end connection area and the nylon bearing connections), which corroborated with real-test observations.

3.2 Vertical compliance (z)

In Figure 6, the system deformation (solid line) is shown for the z direction. Under compressive ($O - A$) and tensile ($O - B$) loading, the system exhibited a similar quasi linear elastic load path (i.e., $u_z = F_z/K_z$) after correcting for the rigid sample deformation and movement. Under compressive loading ($O - A$), a spring stiffness of $K_{lz,-} = 1237$ N/mm was observed, which corresponded to a deformation of $u_{z,-} = 3.28$ mm at $F_{z,-} = 3200$ N, roughly three times greater than the numerical result ($u_{z,a+b} = 1.14$ mm).

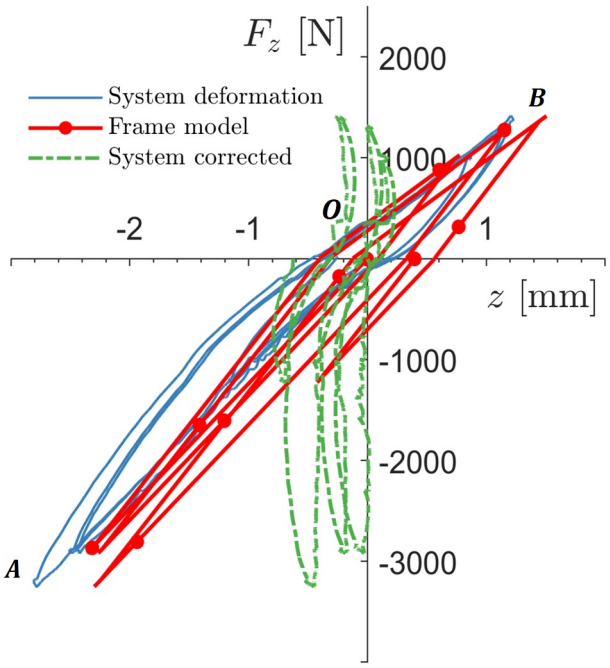

Figure 6: System deformation,frame model, and corrected system deformation for the z direction

The difference in the FE analysis and vertical compliance test can be explained in terms of the adopted simplifications, as discussed previously. Nevertheless, the FE displacement contours, shown in Figure 5, corroborated with the observed deformation zones during the compliance test, namely at the rigid box structure, which was associated with deformation of the nylon bearings on the vertical linear motion guides. In tension ($O - B$), a stiffness of $K_{lz,+} = 866.50$ N/mm was derived and a maximum deformation of $u_{z,+} = 1.23$ mm occurred at $F_{z,+} = 1200$ N. During unloading to the origin from the maximum compressive load $F_{z,-}$ ($A - O$), minimal nonlinear behaviour was exhibited, accumulating a residual displacement of $a_{z,-} = 0.46$ mm. In the tensile unload regime ($B - O$), this was similar but only a nominal residual displacement of $a_{z,+} = 0.05$ mm was accumulated. This was because $a_{z,-}$ and $a_{z,+}$ were recovered when loading in the opposing direction, consistent with the kink observed during compressive and tensile loading in the first 200 N. This was associated with movement of the rigid box caused

by deformation of the nylon guide bearings, as identified in the FE analysis and in video footage of the actual tests (Riccio & Ciantia, 2024). After four cycles, the system's response remained consistent, minimal hysteresis was exhibited, and the unload paths showed a consistent approximate linear stiffness of $(A-O)$ $K_{ulz,-} = 1499.25$ N/mm and $(B-O)$ $K_{ulz,+} = 1543.20$ N/mm. In Figure 6, the expected response using a linear model (as defined in equation 2) is shown by the line with dotted markers, whereas the resulting system correction corresponds to the dashed line.

3.3 Horizontal compliance (x)

In the x direction, loading was limited due to the fixity condition of the rod end connection which prevented rotation (see Figure 4). The system deformation (solid line) is shown in Figure 7 and indicated a quasi-linear-elastic response over the load and unload range $(O-A-O)$ $F_{x,+} = 158$ N, $(O-B-O)$ $F_{x,-} = -171.$ N. The same response exhibited in Figure 7 was observed for other higher loading tests ($F \approx 250$ N).

The compliance was modelled by a linear spring model (see Figure 7, line with dotted markers) and the system was corrected using Equation 1) in both directions, where $K_{x,+,-} = 303.00$ N/mm. This was effective in removing system deformation, as demonstrated in Figure 7 (dashed line u_x^{corr}).

$$u_x^{corr} = u_x - F_x/K_{x,+,-} \tag{1}$$

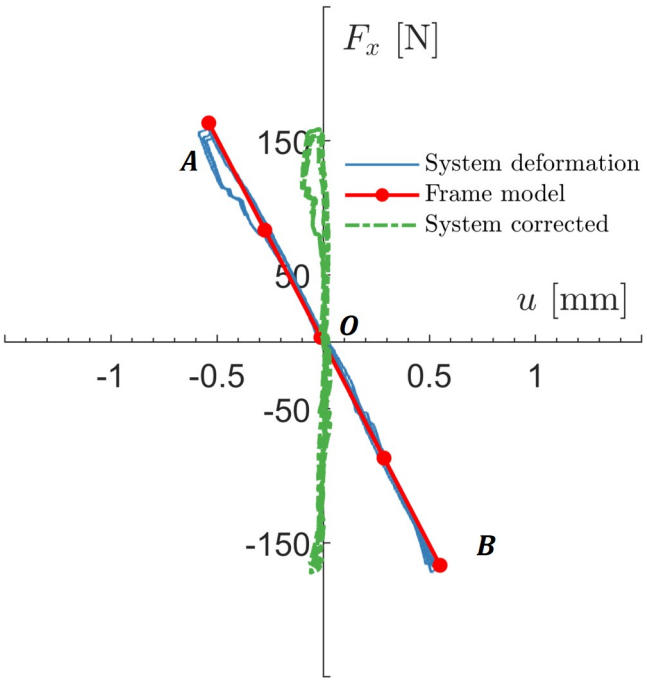

Figure 7: System deformation, frame model and corrected system deformation for the x direction

3.4 Horizontal compliance (y)

In the y direction, a quasi-linear elastic load and non-linear elastic unload response in both directions was observed (see Figure 8a, dashed line). Local displacement measurements at location (i), shown in Figure 4a, indicated that the deformation was concentrated in the slender connection between the rod end and the load cell, behaving as a fixed-free beam. Still, most of the initial non-linear response was due to the deformation of the "rigid" sample to

plate fixing, as confirmed by the sensor mounted on the clevis joint (location ii, see Figure 8a). After correcting for this, the system response became almost fully linear at low load levels, as demonstrated by the solid line in Figure 8a. This reduced the maximum displacement by approximately 50 %, to values of $(O-A)$ $u_{y,+} = 1.55$ mm at $F_{y,+} = 400$ N and $(O-B)$ $u_{y,-} = 1.93$ mm at $F_{y,-} = 400$ N. After 4 cycles, the system's response remained the same indicating elasticity and negligible drift or hysteresis.

Correction for the frame stiffness during loading was achieved by adopting two different elastic springs for each direction of loading, namely $(O-A)$ $K_{y,l,+} = 181.16$ N/mm and $(O-B)$ $K_{y,l,-} = 183.15$ N/mm, as shown in Figure 8b by the line with circle markers. For unloading, the frame behaved linearly above $\approx$ 100N in both directions but became strongly non-linear toward the load origin. For simplicity, the unload behaviour was captured using a linear model with $K_{y,ul,+} = 308.60$ N/mm and $(B-O)$ $K_{y,ul,-} = 322.58$ N/mm. Furthermore, rather than including a force-dependent non-linear stiffness, above $F_{max} = 400$ N, the linear unload stiffness was corrected to return to the target residual displacement as outlined in Equation 2. Application of the model in accounting for compliance was demonstrated by the dashed-line in Figure 4b.

$$u_{z,y}^{corr} = \begin{cases} u_{z,y} - F_{z,y}/K_{ref} & \text{if } F_p < F_{max} \\ u_{z,y} - F_{z,y}/K_{ref} \cdot F_{max}/F_p & \text{if } F_p > F_{max} \end{cases} \tag{2}$$

where K_{ref} is the elastic unload spring stiffness defined by the compliance tests for the y and z directions, F_p is the compliance-exceeding force during testing and F_{max} is the max compliance test load.

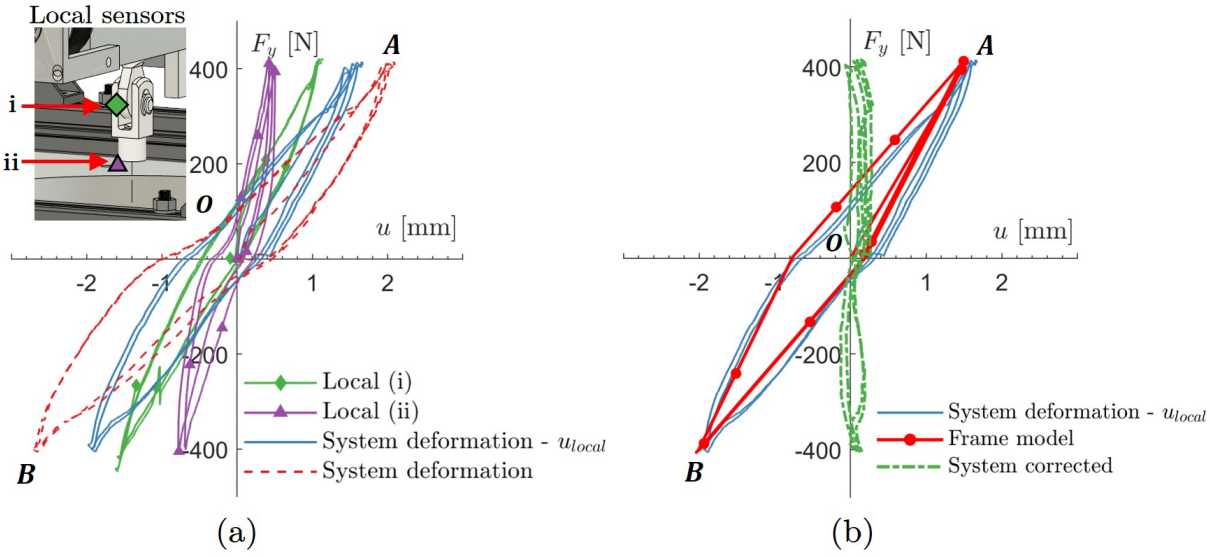

Figure 8: Frame compliance for y direction showing (a) system deformation and system deformation corrected for local displacement and (b) system deformation corrected for local displacement, frame model, and corrected system deformation

4 System limits and PID performance

The frame was controlled using the graphical interface coding language LabVIEW (National Instruments, 2023). This was facilitated by a National Instruments (NI) compact-RIO chassis 9045 combined with 3No. I/O modules (NI 9263, NI 9482, and NI 9202) for analogue DC voltage control, computer-controlled relaying, and data

acquisition, respectively. Four quadrant, linear output motor controllers were used as an intermediate between the signal voltage (from the NI 9263) and the motors, improving the low-speed control. The system was developed to be capable of both displacement and load control by means of proportional-integral-derivative (PID) control, a widely used technique for closed-form feedback control. To tune the PID parameters during testing, an automatic tuning PID provided by LabVIEW was used. In this instance it was able to overcome challenges associated with poor PID control and error range (Åström & Hägglund, 1995; Khan et al., 2015), operating similarly to self-tuning PID controllers, e.g., Alia et al. (2011). This was preferable given variability and evolving test conditions (i.e., soil/rock stiffness evolution). The system was operated at 50 Hz to maintain good feedback performance for the PID operation as well as adequate sensor read rate, to avoid aliasing issues arising from under sampling (Nyquist, 1928). In Figure 9, examples of the system response are given. Displacement control (exemplified by the z direction) indicated consistent performance with negligible stabilisation time for displacement rates between (A) 0.02 mm/s and (D) 0.3 mm/s under variable loads, as evidenced by the example for A (see Figure 9a). In Figure 9b, cyclic load control was demonstrated via time (T)- cyclic force (F_{cyc}) results for the y direction by means of one-way and partial one-way inputs (i.e., force does not return to zero). These stages highlighted the adaptability of the system to load and frequency demand and further so when observing the maximum standard deviation (SD) of cycle peak loads, which was low, ranging from 4.73E-04 (low load range) to 0.0466 (high load range). The higher SD was attributed to the small number of cycles performed in the high load range, which included the initial low-level disturbance caused by the change in frequency and load. Cyclic displacement performance was investigated (see Figure 9c) by means of one- and two-way T-cyclic displacement (u_{cyc}) stages, performed using the z and x direction at low and high displacement requests. Here, the system appeared to perform well to varied cyclic displacement and frequency requirements. Minor error was demonstrated by the SD of the cycle peak displacement, which ranged from 0.0248 (u_{cyc} = ± 0.88 mm) to 0.041 (u_{cyc}= -5.1 mm). The system performance and operational limits are summarised in Table 2, noting that that the performance was subject to test set up and PID performance. Such limits and errors experienced could be overcome by using more sophisticated motors capable of speed control or by adopting a more efficient feedback system.

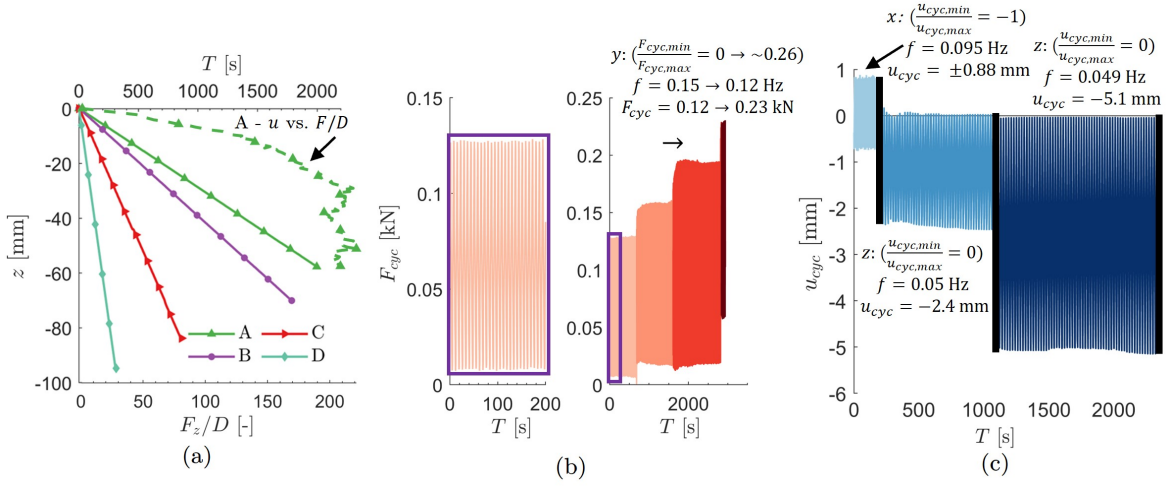

Figure 9: System performance for example tests. (a) displacement control in the vertical direction, (b) partial 1-way cyclic load control in the horizontal pivot- direction (y), and (c) one- and two-way displacement control in the vertical (z) and non-pivot horizontal (x) direction

Table 2: System performance

System limit	z	x	y
u (mm)	120	100	100
Load (N)	5000	150-500	150-500
u rate (mm/s)	0.02-0.4	0.02-0.1	0.02-0.4
Cyclic Frequency (Hz)	0.05-0.2	0.01-0.08	0.05-0.2
Load accuracy		±0.25%	
u accuracy		±0.2%	

For additional resources pertaining to the frame's construction, operation and control system, reference can be made to the system's manual as well as a series of instructional videos on the frame's operation which are available at the repository, see Riccio & Ciantia (2024).

5 System application

After the system had been studied for compliance and the PID servo control was configured, an extensive small scale pile test program was undertaken. Two of the preliminary pile tests conducted during assessment of the PID control on loose and dense sand samples are presented here for demonstrative purpose. These first tests involved installation of a pile to a depth of 100 mm at a rate of 0.1 mm/s, which was then subjected to a large displacement lateral monotonic push at the pile head (y direction). In both tests, in-test radiography (IR) monitored the pile and soil behaviour in the configuration shown in Figure 10.

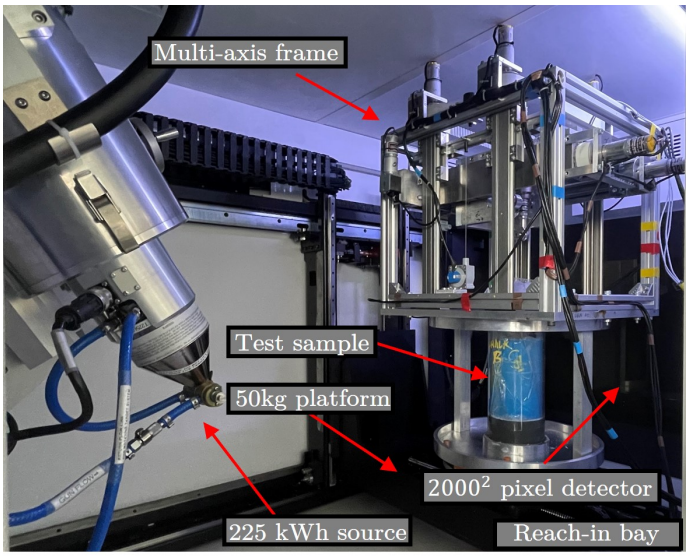

Figure 10: Multi-axis frame stationed in the University of Dundee Nikon XTH 225 CT Scanner

5.1 Material and preparation

5.1.1 Specimen preparation

HST-95 sand, whose properties can be found in Lauder et al. (2013), was used for these first tests. Samples were dry pluviated using an automatic hopper to achieve a certain relative density (R_d), and uniformly fill the

small chamber to a height of approximately 280 mm. Different aperture widths were used to achieve both dense ($R_d = 80$–85 %) and loose ($R_d = 40$–45 %) states.

5.1.2 Pile properties

An OE pile of outer diameter $D \approx 15.37 \pm 0.02$ mm and wall thickness $t_w \approx 0.86 \pm 0.02$ mm, fabricated from stainless steel (bending stiffness $E_p \approx 202.5 \pm 12.5$ GPa and $E_p \cdot I \approx 0.21 \pm 0.0155$ kNm^2), was selected to perform these tests. The pile aspect ratio $L/D \approx 15$ suggested a slender pile and the pile relative stiffness of $K_R \approx 0.024 \pm 0.002$ (see Equation 3) (Abadie et al., 2019; Poulos & Hull, 1989) suggested that it would exhibit a quasi-flexible behaviour in the case of the dense sand, following a slight push beyond the initial penetration depth to ≈ 115 mm.

$$K_R = \frac{E_p \cdot I}{E_s \cdot L^4} \quad \begin{matrix} \text{for } K_R > 0.208 \text{ (Rigid)} \\ \text{for } K_R < 0.0025 \text{ (Slender)} \end{matrix} \tag{3}$$

where E_s is the Young's modulus at the pile tip, based upon an estimated soil modulus of dense sand ($E_s = 50$ MPa) obtained from Abadie (2015) and I is the piles' second moment of area.

5.1.3 Scaling limitations

Two major challenges in physical modelling are scaling and boundary effects (Albiker et al., 2017; Schnaid & Houlsby, 1991). On one side, down scaling the structure alters the grain size to structure ratio; on the other, increased proximity to boundaries can introduce adverse failure mechanisms. In these preliminary tests, no specific scaling to achieve similitude with field-scale pile sizing was applied, nonetheless grain scale effects were deemed negligible as pile diameter to mean grain size $D/D_{50} \approx 118$ (> 88) (Klinkvort, 2012). Despite this, some effects of the $1g$ stress-level were unavoidable and likely contributed to some of the artefacts discussed in the test observations, such as stress-dependent dilatancy and stiffness associated with granular materials (LeBlanc et al., 2010; Albiker et al., 2017). The specimen to chamber diameter ratio ($D_s/D \approx 8$) was approximately 6.5 times lower than is typically assumed to avoid excessive boundary effects (≈ 50) (Schnaid & Houlsby, 1991; Alvarez-Borges et al., 2022a). Having said that, Albiker et al. (2017) performed a series of $1g$ small-scale lateral pile tests with a D_s/D ratio of 10 observing limited boundary effects at loads < 50 % of the pile capacity, which is consistent with observations in Klinkvort et al. (2018) for centrifuge testing. Compared to the small chamber configuration, the large diameter Perspex chamber would offer an improved D_s/D ratio (≈ 20 in this case), which would likely reduce the boundary effect considerably, albeit reducing X-ray penetration and increasing imaging artefacts (Alvarez-Borges et al., 2022a). Additionally, constraining the ground surface with an initial top overburden and utilising low R_d samples are two ways that help avoid excessive dilatancy and high friction angle artefacts (LeBlanc et al., 2010).

5.2 In-test radiography

IR was performed using the 225-kWh X-ray source at the University of Dundee set to a voltage of 200 kV and current of 180–300 μA. Exposure time ranged from 1 to 4 s. Radiograph images had a resolution of 2000^2 pixels, offering a pixel-to-millimetre resolution of ≈ 0.128 mm. Imaging analysis was used to track pile and soil displacements through grey-scale intensity (attenuation) in the X-ray radiographs by means of a modified version

of the Canny edge detector (Canny, 1986). Soil level inside the penetrating pile was also studied and captured, where possible, by analysing the gradient of the horizontal mean intensity.

5.3 Jacked installation observations

Figure 11a shows pile head load (F_z) versus normalised penetration (L_z/D), whereas Figure 11b shows the normalised plug position (P_z/D) for the dense and loose cases throughout the penetration, where AGL is above ground level and BGL is below ground level. The loose case maintained a low and gradual linear load growth (F_z^{loose}) throughout penetration, which was indicative of limited shaft and base resistance and ease of material displacement, whereas the dense case exhibited exponential load growth (F_z^{dense}) with depth. This was with the exception of a load drop at $L_z/D \approx 3.2$, which was attributed to a brief pause in testing caused by PID controller training. At the maximum L_z/D, F_z^{dense} was approximately $9F_z^{loose}$, which was assumed to be in part caused by the increased shaft friction as a result of increased radial stress, in line with Paik et al. (2003), but fundamentally was thought to be associated with an increased end bearing resistance. The latter can be induced by changes in pile basal area, i.e., pile plugging (Lehane & Gavin, 2001; Zheng et al., 2020), and occurs when the frictional resistance on the inner pile exceeds the end bearing resistance required to displace the material ahead of the pile. The aforementioned mechanism leads to a wedge of soil forming near the tip, where the material is more densely packed as a result of arching, dilation, and principal stress rotations (Liu et al., 2022b) and which is more marked as pile diameter reduces (Cerfontaine et al., 2023; Zheng et al., 2020). The phenomenon of plugging in granular materials at small scale has previously been identified by way of physical measurement (Lehane & Gavin, 2001; Gavin & Lehane, 2003), X-ray XCT at stages throughout installation (Kikuchi et al., 2008), and image analysis paired with transparent soils (Zheng et al., 2020; Liu et al., 2022a), but, to the authors' best knowledge, never had IR been used to track plug progression. The method enabled time-resolved displacement tracking of the pile (L_z) and plug position (P_z), with respect to the initial ground level (GL), as well as changes to the GL throughout the tests.

P_z is shown in Figure 11b, which confirmed that in both cases, plug formation occurred in a manner illustrated for the dense case by means of discrete radiographs at key penetration depths (1–4, see Figure 12). In the dense case, this corresponded with the hyperbolic load profile $F_{dense,z}$, analogous to observations drawn by Kikuchi et al. (2008) and Paik et al. (2003) in similar test conditions. The loose case exhibited plugging that occurred more rapidly than the dense sample, indicating that the lower Rd may have been conducive to plugging and which was supported by the final plug heights, which for the dense case was $P_z = 70.82$ mm and for the loose case was $P_z = 61.79$ mm. The faster plugging occurrence of the loose case was hypothesised to be a result of inevitable densification of the plug material, which contrasted the less dense zone ahead of the pile and which was supported by the quasi-constant force-displacement curve. In other words, minimal end bearing growth occurred upon plugging since the pile displaced more freely through the loose grains. Load-penetration and plugging characteristics for both the dense and loose case broadly aligned with observations drawn from tests performed in transparent soils ($D = 14$–25 mm, $t_w = 2$ mm, $R_d = 58$–76 %) (Liu et al., 2022a), as shown in Figure 11a and b. That is, higher jacking forces were observed in a denser sand state and plugging was more rapid for a loose sand state but was not apparent in the jacking force response. This also aligned with Paik et al. (2003) who observed that plugging rates decreased as Rd increased. Although the same trends were drawn in this study, the comparisons to Liu et al. (2022a) were qualitative, and variations in D, R_d, granular fabric, and pile roughness likely led to the faster

plugging observed in in both cases presented by Liu et al. (2022a).

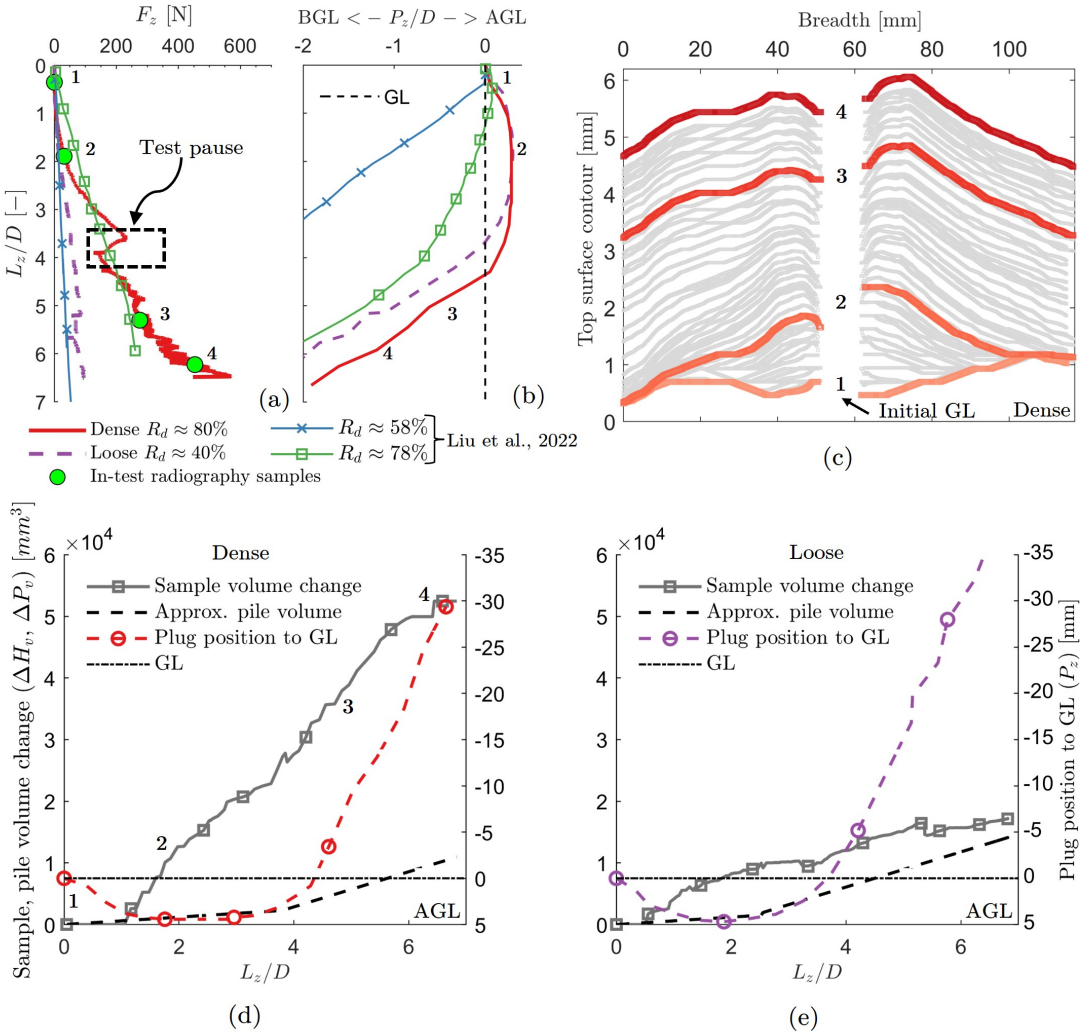

Figure 11: (a)$F - (L_z/D)$ response for loose and dense sand marked with IR samples (1–4); (b) normalised penetration and plug position (data smoothed by a moving mean) compared with Liu et al. (2022a); (c) sample top surface evolution in mm during installation for dense sand; and sample and pile volume change and plug position relative to GL versus normalised penetration depth for (d) dense sand and (e) loose sand. Note: IR samples 1, 2, 3, 4 on Figure parts A–D are associated with the radiographs shown in Figure **??**

Heave level was also studied to understand dilation and volume change during pile installation. Results from this study can be seen in Figure 11c, Figure 11d-e and Figure 12, which include (1) the top surface contours for the dense case during installation versus penetration, (2) the assumed symmetrical sample and pile volume accounting for the tubular steel basal area changes upon plugging (ΔH_v, ΔP_v) and plug position (P_z) versus L_z/D, and (3) discrete radiograph images at points 1, 2, 3, and 4 for the dense case, respectively.

For the dense case, ΔH_v grew rapidly with pile penetration and was most marked after the plugging commenced (i.e., the P_z inflexion point, Figure 11d). At the end of installation, the dense case was $\Delta H_v \approx 3.3 P_v$ and ΔH_v was almost 6 times greater than the loose case, indicating a highly dilatant response due to the increased R_d (Abadie, 2015; LeBlanc et al., 2010). This was further illustrated by the top contour profile growth in Figure 11c and Figure 12 during stages 1–4. This behaviour was not identified in the loose case, which exhibited a ΔH_v that was analogous to the approximated pile volume (ΔP_v) (see Figure 11e). The dilatancy effects observed in the highly

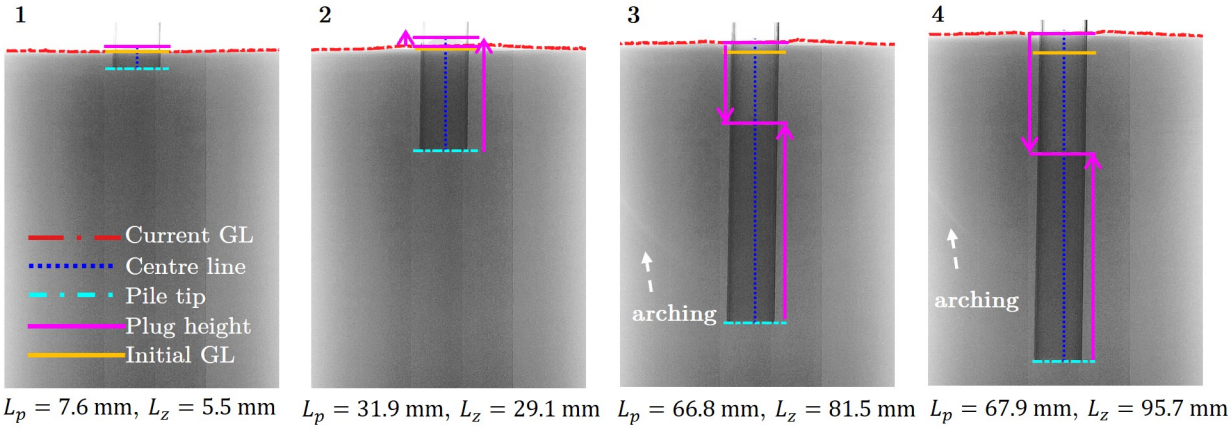

Figure 12: Pile plug, tip, and soil heave tracking via in-test radiography at key stages (1–4) during install of OE pile in dense sand

interlocked dense sample may also have been evidenced by streaks that formed in the discrete radiographs at stage 3– 4 (see Figure 12). The streaks propagated outward from the sample container at 45° after the plugging event commenced (more marked toward the left perimeter, thought to be attributable to slight asymmetry), indicating possible arching between the pile and the sample boundary. This phenomenon was not seen at any point in the loose case, and the media appeared to remain relatively homogeneous. This suggested that, as the R_d was increased, the failure mechanism had a tendency to change from one which allowed relatively free-flow of the sand to that which allowed for stable arching to form (Bi et al., 2020), corresponding with the large sample volume changes and hyperbolic load growth during penetration. These effects were likely intensified by the finite boundaries of the 5-mm-thick small perspex chamber ($D_s = 120$ mm) in which the sample was housed, as well as the lack of sample top confinement, which allowed for excessive dilation in the dense case. Such phenomena are a product of the low mean stress level, a high R_d and friction angle, all of which are intrinsically linked and can be accounted for by careful scaling, as described previously. Because this study was intended to assess the system performance and X-ray application, boundary and fabric issues were less of a concern as the tests did not aim to reliably recreate scaled behaviour. In any case, the experiments revealed characteristics linked to R_d variations and emphasised the importance of the specimen-pile diameter ratio, a criterion that may be satisfied with the large chamber assembly (see Figure 3b).

5.4 Lateral monotonic observations

Figure 13a shows the lateral monotonic pile head load (F_y) versus pile head displacement u_y response for both the loose and dense tests, evidencing the impact of increased R_d. The dense sand exhibited an ultimate capacity (at $0.1D$), approximately twice that of the loose sand.

Regardless of boundary, $1g$ dilation effects and scaling limitations, the IR offered new insights into the failure zone generated ahead of the pile, as exemplified for the dense case. This manifested as a growth in sample height toward the boundary ($\approx$ 0.8 mm) as the pile displaced material in its loading direction. This coincided with a decrease in sample height toward the rear of the pile ($\approx$ 0.2 mm) as the unsupported material fell into the newly formed gap behind the pile, as shown in the ground contour changes in Figure 13b.

IR showed that the pile exhibited a quasi-flexible response during lateral loading in both the loose and dense

cases, which was tracked using the imaging analysis techniques mentioned above exemplified for the dense case (see Figure 14a, b). Given that the piles' deflection (y) and its properties were known, it was possible to tentatively assess the pile behaviour by means of classic Euler-Bernoulli beam theory. Noting that the pile boundary was challenging to track at the ground level (due to the presence of the moving sand-air boundary) and at the tip, due to image noise generated by X-ray imaging artefacts. These missing portions were reconstructed through extrapolation (see Figure 14b), utilising the visible pile portions and frame measured displacement.

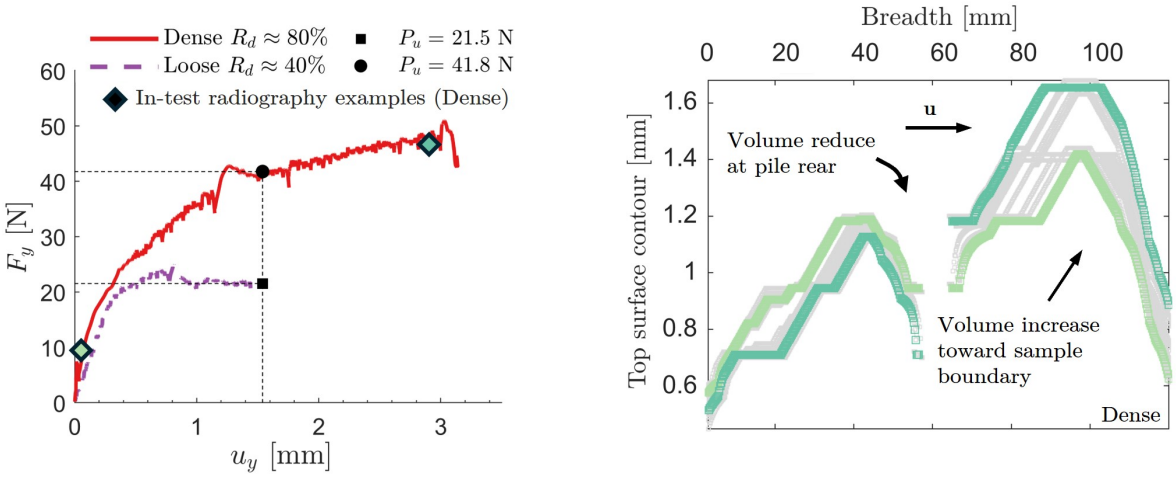

Figure 13: (a) $F_y - u_y$ response for loose and dense sand marked at pile head with key stages marked from the IR (b) Sample top surface change at front and rear of lateral loading direction at key stages for the dense case

Thereafter, a smoothed continuous deflection profile was generated by applying the compressive sampling (CS) method (Zhao & Wang, 2018, 2020) to the composite profile. The CS method overcame some of the challenges associated with fitting high order polynomials to discrete data (Haiderali & Madabhushi, 2016). The method worked by separating the linear and non-linear deflection components, the latter represented by a periodic dataset which improved the smoothness of the data and, if used, high order derivative outputs (d^{2+i}/dz_i^{2+i}) required to obtain moment (M, $i = 0$), shear (V, $i = 1$) and soil resistance (p, $i = 2$), as shown for M in Equation 4.

$$M = \frac{EI \cdot (d^{2+i}(f_L + \hat{f}_{NL}))}{dz_i^{2+i}} \tag{4}$$

where f_L and $\hat{f}_{NL}$ are the linear and nonlinear deflection components along the beam length obtained by the CS method and as above for M, $i = 0$.

The pile bending moment profile derived from Classic Euler Beam theory is shown in Figure 14c. Despite considering possible pile rigidity (EI) variability, the method predicted a bending moment M_{GL} at GL larger than that estimated by the lever-arm from GL to pile head (see Figure 14a,c). A more accurate assessment may have been achieved by using Timoshenko beam theory (Timoshenko & Goodier, 1970), which, for an equivalent deflection profile under certain conditions, predicts a lower peak bending moment (Li et al., 2016). Other sources of error which may have contributed to this overestimation included the radiography image resolution (i.e., the precision of the pile deflection analysis was approximately 0.13 mm), as well as determination of pile rigidity which was not confirmed experimentally.

Nevertheless, these results offered another example of how the frame may be used to assess soil-structure inter-

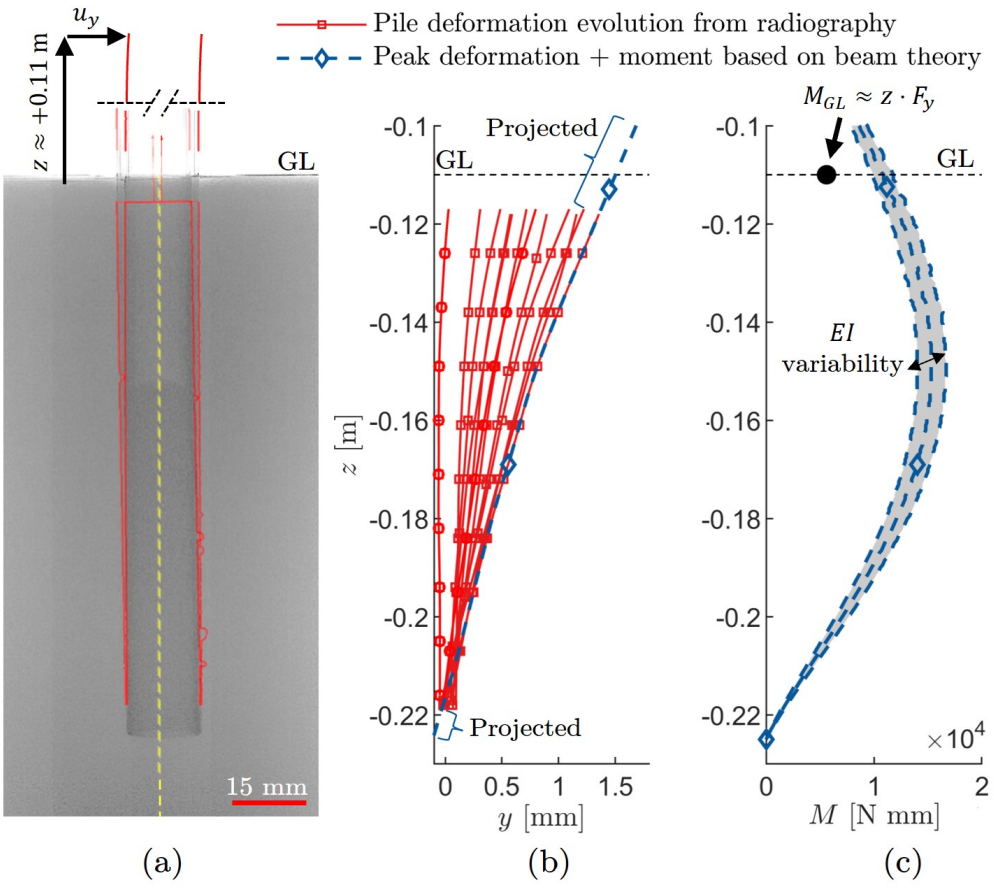

Figure 14: (a) IR image showing initial and peak deflection profiles for dense pile test, (b) subsurface pile deflection from IR translated by initial pile position and extrapolated peak deflection profile, and (c) peak bending moment profile derived via compressive sampled deflection profile and Euler-Bernoulli beam theory. M_{GL} = Pile moment at ground level

action problems. The simple monotonic case presented showed how deflection profiles obtained from radiography can be used to assess the sub-surface behaviour of model piles. With careful scaling, material choice and X-ray set up, the frame could be used to obtain soil-resistance profiles ($p-y$ springs) which are used in standard pile design approaches (API, 2014). Furthermore, since the radiography is time-resolved, the method could be extended to study cyclic $p-y$ performance and associated soil-structure evolution.

6 Other application

The system has also been used to complete a number of work packages related to soil and rock problems (examples include 3D scaled tree-root stability assessments and pile installation and loading in soft rock). These are briefly discussed below.

6.1 3D scaled tree-root stability assessments

Simplified 3D printed tree roots, developed by Zhang et al. (2020b) and Liang (2015), were wished-in-place in HST-95 sand ($R_d = 50\%$) in the large-chamber, as shown in Figure 15a.

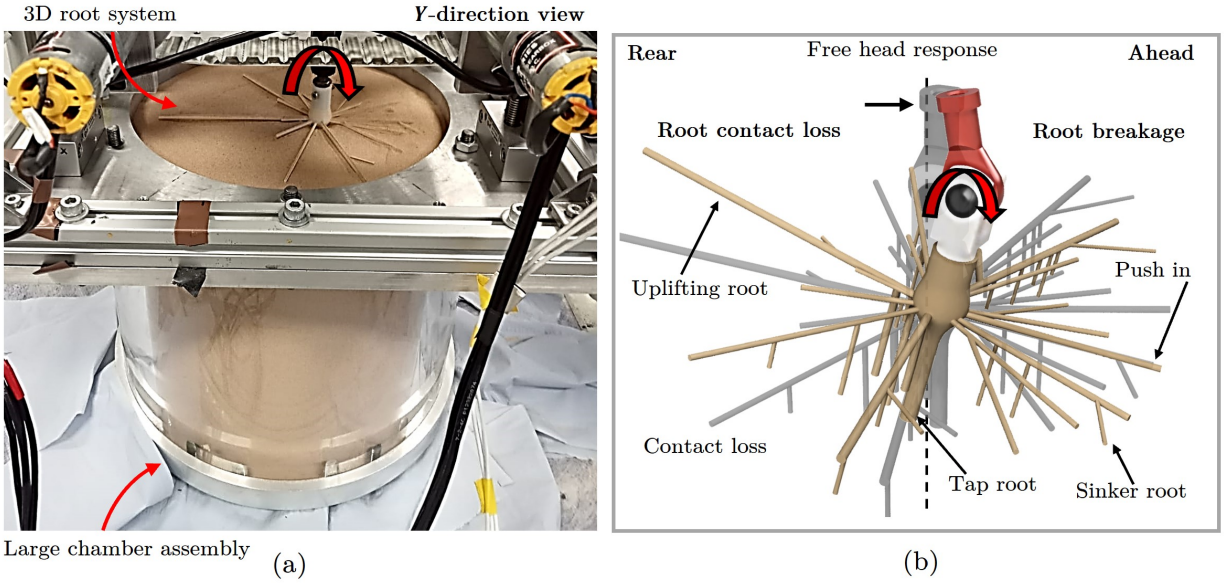

Figure 15: Tree root pushover test. (a) Multi-axis system set up in large chamber mode and filled with pluviated HST-95 sand and (b) tree root model used during the pushover test (redrawn from Zhang et al. (2020b))

A series of compressive, tensile and inclined loading tests were performed to study the root behaviour for comparison to field tests performed at the University of Dundee botanical gardens. A moment-rotation response obtained for one of the monotonic push-over tests during this testing program is shown in Figure 16. The normalised response (where $\theta_{peak} = 9^o$ and M_L is peak moment) exhibited a clear peak before trending to a quasi-constant residual state which experienced local peaks. This was congruent with visual observation of uplifting roots (root contact loss) behind the load direction and breakage of push-in and sinker roots ahead of the loading direction (see Figure 15a and b), similar to the failure mechanisms observed by Zhang et al. (2020b).

The purely one-directional response shown here compared reasonably to field-scale observations (Wessolly & Erb, 2016) ($\theta_{peak} \approx 2^o$) and other small scale studies ($\theta_{peak} \approx 13^o$) (Dattola et al., 2020) offering some confidence in using the analogous small-scale models, despite similar limitations related to scaling mentioned in the previous example. Although a full discussion on the topic is beyond the scope of this article, the multi-directional capability of the system enabled the efficient testing of various loading cases allowing for calibration of a macro-element model in M-V-H space, as discussed in greater detail in Marrazzo et al. (2024).

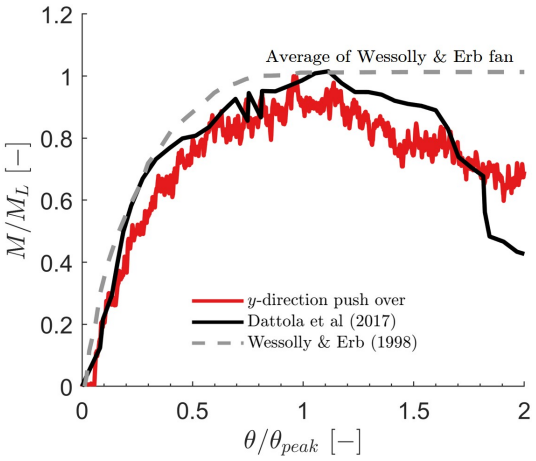

Figure 16: Normalised push-over rotational response versus moment overlaid by the Wessolly & Erb (2016) average field database and prior small-scale test (Dattola et al., 2020)

6.2 ICE-PICK soft rock pile studies

The multi-axis frame has also been used to undertake comprehensive studies on small-scale pile installation, axial and lateral loading, and cyclic behaviour in soft rocks (ICE-PICK). Tests were performed using a range of small-diameter OE piles ($D = 12 - 19$ mm, $t_w \approx 0.7 - 1$ mm), noting that the small-chamber arrangement and specimen to sample diameter ratios were similar to those in the sand tests. Following Alvarez-Borges et al. (2022a), cored soft rock samples were encapsulated in a stiff epoxy resin, characterised by a stiffness of the same order of magnitude as the intact rock. This helped restrain sample deformation during testing. The small chamber size was selected to avoid imaging artefacts associated with low X-ray transmission on large sample sizes, but also for practicality of sample preparation for use within the XCT bay. Although natural intact rock grain sizes cannot be modified, grain-scale effects were assessed to be limited since $D_{50} \approx 5\ \mu m$ and $D/D_{50} \approx 3000$ (> 88) (Albiker et al., 2017), and $t_w/D_{50} \approx 200$ (> 8) (Zhang et al., 2024). Additionally, low-stress level effects on stiffness, dilation, and frictional response, typical of granular materials (LeBlanc et al., 2010), were less relevant in the case of the soft rock because of the highly porous bonded nature of the material (Zheng et al., 2022). Nevertheless, boundary effects were expected to be more pronounced during a plugged installation and this is consistent with crack propagation, which was observed up to the domain boundaries during some of the small-scale tests. Despite this limitation, the experiments still provided real time damage evolution data that could be used to aid validation of numerical models, like those used in ICE-PICK (Ciantia et al., 2024).

These studies, combined with IR and XCT scans (Riccio et al., 2024), have provided valuable insight into changes in rock fabric caused by installation and axial/lateral cyclic pile events. As mentioned above, observations have aided in the validation of numerical models (Previtali et al., 2023) and furthermore have aligned qualitatively with field-scale cases (Jardine et al., 2024; Ciavaglia et al., 2017). An example of one test from the ICE-PICK campaign is shown in Figure 17. XCT 3D (fig.17a) and 2D (Figure 17b) cross sections through an OE pile ($D = 18.95$ mm, $t_w = 0.96$ mm) jacked 60 mm into a soft low-medium density chalk reveal damage induced by the installation process (stage 0, left), and after, the effects of three stages of vertical cyclic displacement at the pile head (stage 3, right). Each stage consisted of different cyclic displacement frequencies and amplitudes to study the effect on degradation of near-pile fabric. Those included: Stage 1 - $f = 0.120$ Hz at $u_{cyc} = 1.4$ mm, Stage 2 - $f = 0.05$ Hz

at $u_{cyc} = 2.5$ mm, Stage 3 - $f = 0.05$ Hz at $u_{cyc} = 2.5 + 5$ mm offset. These are illustrated by normalised peak cycle loads ($F_z/F_{z,peak}$) versus cycle number in Figure 18, where $F_{z,peak}$ is the maximum load exhibited in each stage and F_z are the peak loads associated with each cycle. visualising rock damage as it occurs allows for the tracking of the degradation process, and, in this instance, the effects of vertical cyclic performance are noteworthy. As shown in Figure 18, uplift $F_z/F_{z,peak}$ exhibited a rapid degradation, coinciding with extensive radial damage in the near-pile zone (see Figure 17b, right).

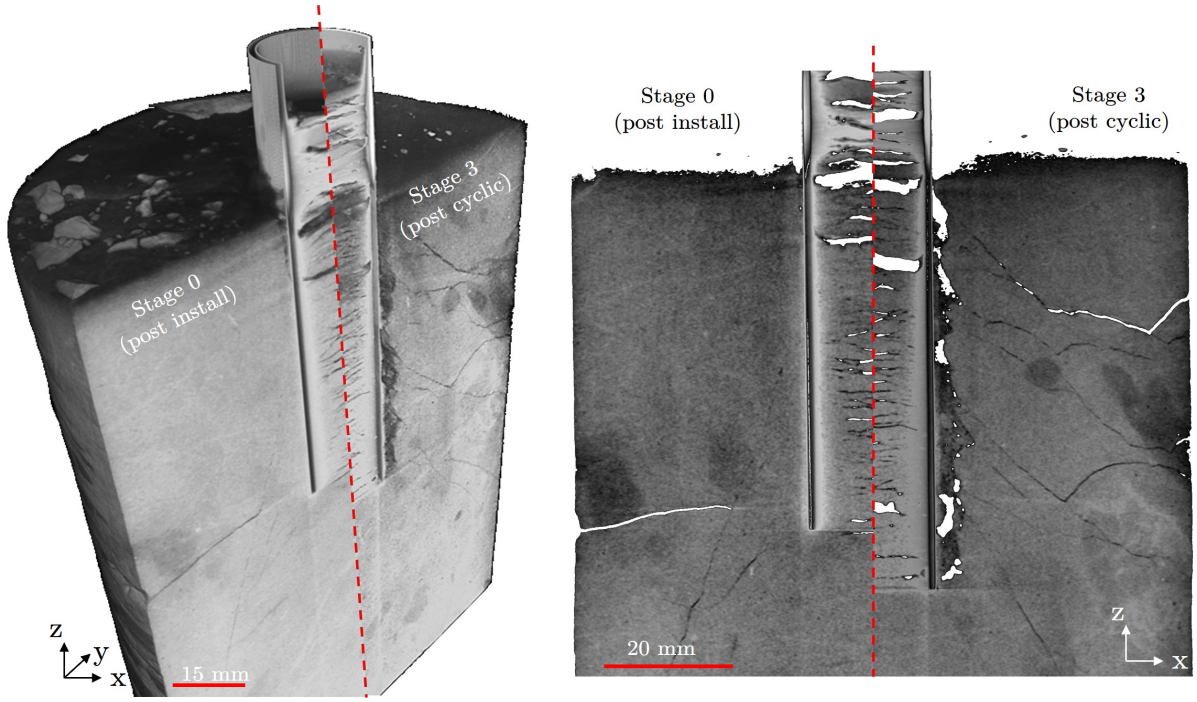

Figure 17: Effects of vertical cyclic displacement on open-end pile performance low-medium density chalk demonstrated by (a) centre-slice 3D CT images after jacked installation (left) and following 3-stages of cyclic displacement (right) (b) 2D slice view point

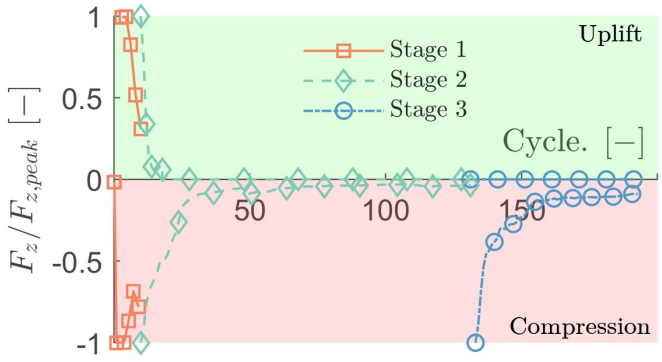

Figure 18: Compressive and tensile normalised force peaks versus cycle number for 3 stages of vertical cyclic displacement testing of a model open-ended pile installed in a low medium density chalk

Outward chalk radial damage from the pile wall increased from approximately $1 - 1.5$ mm to an average of 5 mm after stage 3. This substantial destructured zone ($\approx 8964\ mm^3$) was largely discharged onto the surface of

the chalk sample during the sequence of uplifts, which, along with the intact state of the far-field material, likely contributed to a low radial stress, degrading rapidly as the void space accumulated. Interestingly, the compressive $F_z/F_{z,peak}$ degraded more gradually, which was thought to be the result of constricted material at the tip zone and plug. However, with repeated cycling, the compressive capacity also diminished to zero, possibly due to densification and gap formation at the pile tip zone, a result of using the displacement control cyclic method. In Stage 3, the pile was jacked beyond the initial cycling zones (+5 mm), exhibiting new compressive resistance, since the pile was reacting against more competent material, but which rapidly degraded to near-zero. The latter was thought to be the result of extensive damage around the pile walls. This brief example, part of the broader ICE-PICK experimental program (Riccio et al., 2024), provided insight into the complex mechanical behaviour of soft rock. Additionally, it demonstrated how the multi-axis frame and in-test XCT have been used to evaluate factors contributing to low pile uplift shaft capacity, a feature also observed in previous field and small-scale studies in soft rock (Buckley et al., 2018; Alvarez-Borges et al., 2022a).

7 Conclusion

In this article, the design and development of a new loading frame for use within an XCT bay has been described. A simple pile installation and lateral loading test was used to (a) validate the system performance and (b) demonstrate its potential, while also revealing in-situ mechanisms. Other applications were briefly discussed, highlighting the versatility of the system for studying soil-structure interactions. These included studies on the loading characteristics of 3D printed model scale roots, which have complimented an extensive field-testing program at the University of Dundee botanical gardens, and the behaviour of piles in soft rock, which is assisting in the ongoing ICE-PICK project. It is anticipated that the system could serve as a useful tool for other geotechnical laboratories. In addition, because its compactness allows for real-time radiography and XCT imaging, it could be used in both a teaching and experimental setting to reveal in-situ mechanisms and fundamental principles that could previously only be visualised by conceptualisation. Although boundary effects were observed, it was identified that they could be reduced by modification to the test specimen and chamber set up. Nevertheless, with or without boundary effects, the results may still be used to validate numerical models. In line with the objectives of the ICE-PICK project, these validated numerical models could then be used to investigate full-scale engineering problems. In summary, the system has the potential to enrich learning and reveal new soil or rock-structure interactions, as demonstrated in this article.

8 Acknowledgments

This work is an output from the ICE-PICK project, funded by the EPSRC NIA grant EP/W00013X/1. The authors would like to acknowledge and thank Dr. Scott Robinson for his significant support in the preliminary design phase of the system. Prof. Michael Brown, Craig Davidson, and Dr. Yaseen Sharif are also thanked for their insight and knowledge on control systems and physical testing, whilst Dr. Laszlo Csetenyi is also thanked for his guidance and knowledge on X-ray computed tomography. Additionally, the authors give thanks to the University of Dundee geotechnical, electrical, and mechanical technicians for their continued support throughout the development.

References

Abadie, C. N. (2015). Cyclic Lateral Loading of Monopile Foundations in Cohesionless Soils. *Dissertation*, (p. 236).

Abadie, C. N., Byrne, B. W., & Houlsby, G. T. (2019). Rigid pile response to cyclic lateral loading: Laboratory tests. *Geotechnique*, *69*, 863–876. doi:10.1680/jgeot.16.P.325.

Albiker, J., Achmus, M., Frick, D., & Flindt, F. (2017). 1 G Model Tests on the Displacement Accumulation of Large-Diameter Piles Under Cyclic Lateral Loading. *Geotechnical Testing Journal*, *40*, 173–184. doi:10.1520/GTJ20160102.

Alia, M. A. K., Younes, T. M., & Subah, S. A. (2011). A Design of a PID Self-Tuning Controller Using LabVIEW. *Journal of Software Engineering and Applications*, *04*, 161–171. doi:10.4236/jsea.2011.43018.

Alvarez-Borges, F., Ahmed, S., Madhusudhan, B. N., & Richards, D. (2022a). Investigation of pile penetration in calcareous soft rock using X-ray computed tomography. *International Journal of Physical Modelling in Geotechnics*, *22*, 38–52. doi:10.1680/jphmg.20.00031.

Alvarez-Borges, F., Burca, G., Atwood, R., James, A., Wolstenholme, M., & Ahmed, S. (2022b). Correlative neutron and X-ray tomography imaging of pile installation in chalk. *Geotechnique*, . doi:10.1680/jgeot.21.00318.

API (2014). *API RP2GEO - Geotechnical Foundation Design Considerations (Including amendments to 2021)*. Technical Report American Petroleum Institute (API).

Arshad, M., & O'Kelly, B. C. (2014). Development of a rig to study model pile behaviour under repeating lateral loads. *International Journal of Physical Modelling in Geotechnics*, *14*, 54–66. doi:10.1680/ijpmg.13.00015.

Arshad, M. I., Tehrani, F. S., Prezzi, M., & Salgado, R. (2014). Experimental study of cone penetration in silica sand using digital image correlation. *Geotechnique*, *64*, 551–569. doi:10.1680/geot.13.P.179.

Åström, K. J., & Hägglund, T. (1995). PID controllers: theory, design, and tuning. *IEEE Control Systems Magazine*, *2*.

Autodesk (2023). Autodesk: Fusion 360. URL: https://web.archive.org/web/20240514141427/https://www.autodesk.co.uk/products/fusion-360/overview.

Bi, Z., Gong, Q., Guo, P., & Cheng, Q. (2020). Experimental study of the evolution of soil arching effect under cyclic loading based on trapdoor test and particle image velocimetry. *Canadian Geotechnical Journal*, *57*, 903–920. doi:10.1139/cgj-2019-0205.

Bosch Rexroth (2023). Bosch Rexroth Strut Profile (30x30). URL: https://web.archive.org/web/20240514141709/https://www.boschrexroth.com/en/gb/products/product-groups/assembly-technology/.

Breco-flex (2023). Brecoflex reinforced polymer belts. URL: https://web.archive.org/web/20240514141901/https://www.brecoflex.com/.

Buckley, R. M., Jardine, R. J., Kontoe, S., Parker, D., & Schroeder, F. C. (2018). Ageing and cyclic behaviour of axially loaded piles driven in chalk. *Geotechnique*, *68*, 146–161. doi:10.1680/jgeot.17.P.012.

Bull, D. J., Smethurst, J. A., Sinclair, I., Pierron, F., Roose, T., Powrie, W., & Bengough, A. G. (2020). Mechanisms of root reinforcement in soils: An experimental methodology using four-dimensional X-ray computed tomography and digital volume correlation. *Proceedings of the Royal Society A: Mathematical, Physical and Engineering Sciences*, *476*. doi:10.1098/rspa.2019.0838.

Canny, J. (1986). A Computational Approach to Edge Detection. *IEEE Transactions on Pattern Analysis and Machine Intelligence*, *PAMI-8*, 679–698. doi:10.1109/TPAMI.1986.4767851.

Castellanza, R., Parma, M., Pescatore, V., & Silvestro, G. (2009). Model footing load tests on soft rocks. *Geotechnical Testing Journal*, *32*, 262–272. doi:10.1520/gtj101845.

Cerfontaine, B., Ciantia, M., Brown, M., White, D., & Sharif, Y. (2023). DEM study of particle scale effect on plain and rotary jacked pile behaviour in granular materials. *Computers and Geotechnics*, *161*, 105559. doi:10.1016/j.compgeo.2023.105559.

Cheng, Z., Wang, J., Coop, M. R., & Ye, G. (2020). A miniature triaxial apparatus for investigating the micromechanics of granular soils with in situ X-ray micro-tomography scanning. *Frontiers of Structural and Civil Engineering*, *14*, 357–373. doi:10.1007/s11709-019-0599-2.

Ciantia, M., Zheng, J., Previtali, M., & Knappett, J. (2024). Simulation of pile installation in chalk: discrete and continuum approaches. In *XVIII European Conference on Soil Mechanics and Geotechnical Engineering*. Lisbon.

Ciantia, M. O., Castellanza, R., & Fernandez-Merodo, J. A. (2018). A 3D Numerical Approach to Assess the Temporal Evolution of Settlement Damage to Buildings on Cavities Subject to Weathering. *Rock Mechanics and Rock Engineering*, *51*, 2839–2862. doi:10.1007/s00603-018-1468-3.

Ciavaglia, F., Carey, J., & Diambra, A. (2017). Monotonic and cyclic lateral tests on driven piles in Chalk. *Proceedings of the Institution of Civil Engineers: Geotechnical Engineering*, *170*, 353–366. doi:10.1680/jgeen.16.00113.

Cnudde, V., & Boone, M. N. (2013). High-resolution X-ray computed tomography in geosciences: A review of the current technology and applications. *Earth-Science Reviews*, *123*, 1–17. doi:10.1016/j.earscirev.2013.04.003.

Dattola, G., Ciantia, M. O., Galli, A., Blyth, L., Zhang, X., Knappet, J. A., Castellanza, R., Sala, C., & Leung, A. K. (2020). A Macroelement Approach for the Stability Assessment of Trees. In *Lecture Notes in Civil Engineering* (pp. 417–426). Springer International Publishing volume 40. doi:10.1007/978-3-030-21359-6{_}44.

Davidson, C., Brown, M. J., Cerfontaine, B., Al-Baghdadi, T., Knappett, J., Brennan, A., Augarde, C., Coombs, W., Wang, L., Blake, A., Richards, D., & Ball, J. D. (2022). Physical modelling to demonstrate the feasibility of screw piles for offshore jacket-supported wind energy structures. *Geotechnique*, *72*, 108–126. doi:10.1680/jgeot.18.P.311.

Desrues, J., Andò, E., Mevoli Ando, F. A., Debove, L., & Viggiani, G. (2018). How does strain localise in standard triaxial tests on sand: Revisiting the mechanism 20 years on. *Mechanics Research Communications*, *92*, 142–146. doi:10.1016/j.mechrescom.2018.08.007.

Doreau-Malioche, J., Combe, G., Viggiani, G., & Toni, J. B. (2018). Shaft friction changes for cyclically loaded displacement piles: An X-ray investigation. *Geotechnique Letters*, *8*, 66–72. doi:10.1680/jgele.17.00141.

Ferreira, T. R., Pires, L. F., & Reichardt, K. (2022). 4D X-Ray Computed Tomography in Soil Science: an Overview and Future Perspectives at Mogno/Sirius. *Brazilian Journal of Physics*, *52*. doi:10.1007/s13538-021-01043-x.

Gavin, K. G., & Lehane, B. M. (2003). The shaft capacity of pipe piles in sand. *Canadian Geotechnical Journal*, *40*, 36–45. doi:10.1139/t02-093.

Haiderali, A. E., & Madabhushi, G. (2016). Evaluation of Curve Fitting Techniques in Deriving p – y Curves for Laterally Loaded Piles. *Geotechnical and Geological Engineering*, *34*, 1453–1473. doi:10.1007/s10706-016-0054-2.

IGUS (2023). IGUS Linear guide rails. URL: https://web.archive.org/web/20240702192913/https://www.igus.co.uk/info/drylin-linear-systems.

Jardine, R. J., Buckley, R. M., Liu, T., Andolfsson, T., Byrne, B. W., Kontoe, S., Mcadam, R. A., Schranz, F., & Vinck, K. (2024). The axial behaviour of piles driven in chalk. *Géotechnique*, *74*, 553–569. URL: https://www.icevirtuallibrary.com/doi/10.1680/jgeot.22.00041. doi:10.1680/jgeot.22.00041.

Karatza, Z., Andò, E., Papanicolopulos, S. A., Viggiani, G., & Ooi, J. Y. (2019). Effect of particle morphology and contacts on particle breakage in a granular assembly studied using X-ray tomography. *Granular Matter*, *21*, 1–13. doi:10.1007/s10035-019-0898-2.

Khan, M. R., Khan, A. A., & Ghazali, U. (2015). Speed Control of DC Motor under Varying Load Using PID Controller. *International Journal of Engineering*, *9*, 38–48.

Kikuchi, Y., Morikawa, Y., & Sato, T. (2008). Plugging mechanism in a vertically loaded open-ended pile. In *Proceedings of the 2nd BGA International Conference on Foundations, 2008* (pp. 169–180). IHS BRE Press volume 1st.

Klinkvort, R. (2012). *Centrifuge modelling of drained lateral pile-soil response Application for offshore wind turbine support structures*. Ph.D. thesis University of Denmark.

Klinkvort, R. T., Black, J. A., Bayton, S. M., Haigh, S. K., Madabhushi, G. S., Blanc, M., Thorel, L., Zania, V., Bienen, B., & Gaudin, C. (2018). A review of modelling effects in centrifuge monopile testing in sand. *Physical Modelling in Geotechnics*, *1*, 719–724. doi:10.1201/9780429438660-108.

Larsson, E., Gürsoy, D., & Hall, S. A. (2023). Kitchen-based light tomography - a DIY toolkit for advancing tomography - by and for the tomography community. *Tomography of Materials and Structures*, *1*, 100001. doi:10.1016/j.tmater.2022.100001.

Lauder, K. D., Brown, M. J., Bransby, M. F., & Boyes, S. (2013). The influence of incorporating a forecutter on the performance of offshore pipeline ploughs. *Applied Ocean Research*, *39*, 121–130. doi:10.1016/j.apor.2012.11.001.

LeBlanc, C., Houlsby, G. T., & Byrne, B. W. (2010). Response of stiff piles in sand to long-term cyclic lateral loading. *Geotechnique*, *60*, 79–90. doi:10.1680/geot.7.00196.

Lehane, B. M., & Gavin, K. G. (2001). Base Resistance of Jacked Pipe Piles in Sand. *Journal of Geotechnical and Geoenvironmental Engineering*, *127*, 473–480. doi:10.1061/(asce)1090-0241(2001)127:6(473).

Li, P., Du, S., Wang, Y., & Zhao, H. (2016). Timoshenko beam solution for the response of existing tunnels because of tunneling underneath. *International Journal for Numerical and Analytical Methods in Geomechanics*, *40*, 766–784. URL: https://onlinelibrary.wiley.com/doi/10.1002/nag.2426. doi:10.1002/nag.2426.

Liang, T. (2015). *Seismic performance of vegetated slopes*. Ph.D. thesis University of Dundee.

Liu, C., Tang, X., Wei, H., & Zhao, H. (2022a). Visualization Investigation of the Plugging Effect on Open-Ended Pipe Pile Jacked in Transparent Sand. *International Journal of Geomechanics*, *22*, 1–12. doi:10.1061/(asce)gm.1943-5622.0002455.

Liu, T., Ahmadi-Naghadeh, R., Vinck, K., Jardine, R. J., Kontoe, S., Buckley, R. M., & Byrne, B. W. (2022b). An experimental investigation into the behaviour of de-structured chalk under cyclic loading. *Géotechnique*, (pp. 1–38). doi:10.1680/jgeot.21.00199.

Marrazzo, G., Ciantia, M., Riccio, T., Galli, A., & Knappett, J. (2024). Multi axis loading tests on a small scale tree root model. In E. S, & C. M (Eds.), *5th European Conference on Physical Modelling in Geotechnics* (p. 10). Delft: ISSMGE.

Mayoral, J. M., Pestana, J. M., & Seed, R. B. (2016). Multi-directional cyclic p-y curves for soft clays. *Ocean Engineering*, *115*, 1–18. doi:10.1016/j.oceaneng.2016.01.033.

McCarel, S., & Beard, R. (1984). Laboratory Investigation on Piles in Calcareous Sediments. *Naval Civil Engineering Lab Port Hueneme CA*, .

MFA Motors (2023). MFA DC Motors. URL: https://web.archive.org/web/20240514141741/https://www.mfacomodrills.com/.

Monforte, L., Arroyo, M., Carbonell, J. M., & Gens, A. (2022). Large-strain analysis of undrained smooth tube sampling. *Geotechnique*, *72*, 61–77. doi:10.1680/jgeot.19.P.354.

Murff, J. D. (1987). Pile Capacity in Calcareous Sands: State if the Art. *Journal of Geotechnical Engineering*, *113*, 490–507. URL: https://ascelibrary.org/doi/10.1061/%28ASCE%290733-9410%281987%29113%3A5%28490%29. doi:10.1061/(ASCE)0733-9410(1987)113:5(490).

National Instruments (2023). What is LabVIEW? URL: https://web.archive.org/web/20240514141631/https://www.ni.com/en/shop/labview.html.

Nyquist, H. (1928). Certain Topics in Telegraph Transmission Theory. *IEEE*, *47*, 617–644. doi:10.1109/T-AIEE.1928.5055024.

Oliynyk, K., Ciantia, M. O., & Tamagnini, C. (2021). A finite deformation multiplicative plasticity model with non–local hardening for bonded geomaterials. *Computers and Geotechnics*, *137*, 104209. doi:10.1016/j.compgeo.2021.104209.

OMEGA (2023). Omega subminature load cell. URL: https://web.archive.org/web/20240514140229/https://www.omega.co.uk/pptst/LCMFD.html.

Otani, J., Pham, K., & Sano, J. (2006). Investigation of Failure Patterns in Sand Due to Laterally Loaded Pile Using X-Ray CT. *Soils and Foundations*, *46*, 529–535. doi:10.3208/sandf.46.529.

Paik, K., Salgado, R., Lee, J., & Kim, B. (2003). Behavior of Open- and Closed-Ended Piles Driven Into Sands. *Journal of Geotechnical and Geoenvironmental Engineering*, *129*, 296–306. doi:10.1061/(asce)1090-0241(2003)129:4(296).

Peng, J. R., Clarke, B. G., & Rouainia, M. (2006). A device to cyclic lateral loaded model piles. *Geotechnical Testing Journal*, *29*, 341–347. doi:10.1520/gtj100226.

Perbawa, A., Gramajo, E., Finkbeiner, T., & Santamarina, J. C. (2019). Global vs local strain measurements in triaxial tests – Implications. In *53rd U.S. Rock Mechanics/Geomechanics Symposium*.

Phillips, D. H., & Lannutti, J. J. (1997). Measuring physical density with X-ray computed tomography. *NDT and E International*, *30*, 339–350. doi:10.1016/S0963-8695(97)00020-0.

Poulos, H. G., & Hull, T. S. (1989). Role of analytical geomechanics in foundation engineering. In *Proceedings of the Congress sponsored by the Geotechnical Engineering Division and the Construction Division. Geotechnical Special Publication No. 22.* January 1989 (pp. 1578–1606). American Society of Civil Engineers.

Previtali, M., Ciantia, M. O., & Riccio, T. (2023). Numerical installation of OE piles in soft rocks within the G-PFEM framework. In *Proceedings of the 10th European Conference on Numerical Methods in Geotechnical Engineering,* (pp. 322–328). London: International Society for Soil Mechanics and Geotechnical Engineering. doi:https://doi.org/10.53243/NUMGE2023-322.

Riccio, T., & Ciantia, M. (2024). ICE-PICK Multi-axis loading frame repository. *DUNDEE DISCOVERY*, . doi:10.20933/100001306.

Riccio, T., Previtali, M., & Ciantia, M. O. (2024). 4D model tests of CPT pile design performance in chalk. In *New Challenges in Rock Mechanics and Rock Engineering - Proceedings of the ISRM Rock Mechanics Symposium, EUROCK 2024* (pp. 613–618). doi:10.1201/9781003429234-90.

Riccio, T., Previtali, M., Ciantia, M. O., & Brown, M. J. (2023). P-y Response in Porous Rock: Numerical Derivation With Experimental Validation. In *9th International SUT OSIG Conference "Innovative Geotechnologies for Energy Transition"* (pp. 1290–1297). London: Society for Underwater Technology. doi:10.3723/saue7586.

Robinson, S., Brown, M. J., Matsui, H., Brennan, A., Augarde, C., Coombs, W., & Cortis, M. (2019). Centrifuge testing to verify scaling of offshore pipeline ploughs. *International Journal of Physical Modelling in Geotechnics*, *19*, 305–317. doi:10.1680/jphmg.17.00075.

Sato, T., Onda, K., & Otani, J. (2018). Development of a new loading test apparatus for microfocus X-ray CT and its application to the investigation of soil behavior surrounding driven open-section piles. *Soils and Foundations*, *58*, 776–785. doi:10.1016/j.sandf.2018.03.004.

Schnaid, F., & Houlsby, G. T. (1991). An assessment of chamber size effects in the calibration of in situ tests in sand. *Géotechnique*, *41*, 437–445. doi:10.1680/geot.1991.41.3.437.

Smith, J., & Augarde, C. (2015). *A review of x-ray computed tomography in geotechnical research*. Technical Report July Durham University. doi:10.13140/RG.2.1.1827.1846.

Su, D. (2012). Resistance of short, stiff piles to multidirectional lateral loadings. *Geotechnical Testing Journal*, *35*. doi:10.1520/GTJ103840.

TE Connectivity (2023). TE Spring pot displacement sensors. URL: https://web.archive.org/web/20240514135551/https://www.te.com/en/product-SP1-12.html.

The Aluminium Association (2015). *Aluminum Design Manual (ADM-2015)*. 2015. The Aluminum Association.

Timoshenko, S. P., & Goodier, J. N. (1970). *Theory of Elasticity*. New York, NY, USA: McGraw-Hill.

Tudisco, E., Andò, E., Cailletaud, R., & Hall, S. A. (2017). TomoWarp2: A local digital volume correlation code. *SoftwareX*, *6*, 267–270. doi:10.1016/j.softx.2017.10.002.

Viggiani, G., Andò, E., Takano, D., & Santamarina, J. C. (2015). Laboratory X-ray tomography: A valuable experimental tool for revealing processes in soils. *Geotechnical Testing Journal*, *38*, 61–71. doi:10.1520/GTJ20140060.

Wessolly, L., & Erb, M. (2016). *Handbook of tree statics and tree control*. Patzer Verlag.

White, D. J., & Bolton, M. D. (2004). Displacement and strain paths during plane-strain model pile installation in sand. *Géotechnique*, *54*, 375–397. doi:10.1680/geot.2004.54.6.375.

Wood, D. M. (2004). *Geotechnical modelling*. April (1st ed.). Oxfordshire: CRC Press. doi:10.1201/9781315273556.

Zhang, X., Knappett, J. A., Ciantia, M. O., Leung, A. K., Wang, H., & Liang, T. (2024). Root size effects on transverse root-soil interactions. *Computers and Geotechnics*, *165*, 105860. doi:10.1016/j.compgeo.2023.105860.

Zhang, X., Knappett, J. A., Leung, A. K., Ciantia, M. O., Liang, T., & Danjon, F. (2020a). Small-scale modelling of root-soil interaction of trees under lateral loads. *Plant and Soil*, *456*, 289–305. URL: https://link.springer.com/10.1007/s11104-020-04636-8. doi:10.1007/s11104-020-04636-8.

Zhang, X., Knappett, J. A., Leung, A. K., Ciantia, M. O., Liang, T., & Danjon, F. (2020b). Small-scale modelling of root-soil interaction of trees under lateral loads. *Plant and Soil*, *456*, 289–305. doi:10.1007/s11104-020-04636-8.

Zhao, T., & Wang, Y. (2018). Interpretation of pile lateral response from deflection measurement data: A compressive sampling-based method. *Soils and Foundations*, *58*, 957–971. doi:10.1016/j.sandf.2018.05.002.

Zhao, T., & Wang, Y. (2020). Differentiation of discrete data with unequal measurement intervals and quantification of uncertainty in differentiation using Bayesian compressive sampling. *Computers and Geotechnics*, *122*, 103537. doi:10.1016/j.compgeo.2020.103537.

Zheng, J., Previtali, M., Ciantia, M., & Knappett, J. (2023). Comparison of continuum (PFEM) and discrete (DEM) approaches for large insertion BVPs in soft rocks. In *VIII International Conference on Particle-Based Methods* (pp. 1–9). Milan: CIMNE. doi:10.23967/c.particles.2023.037.

Zheng, J., Previtali, M., Knappett, J., & M, C. (2022). Coupled DEM-FDM investigation of centrifuge acceleration on the response of shallow foundations in soft rocks. In *Proceedings of the 10th International Conference on Physical Modelling in Geotechnics* (pp. 264–267). ISSMGE.

Zheng, J. H., Qi, C. G., Zhao, X., Wang, X. Q., & Shan, Y. L. (2020). Experimental Simulation on Open-Ended Pipe Pile Penetration Using Transparent Granule. *KSCE Journal of Civil Engineering*, *24*, 2281–2292. doi:10.1007/s12205-020-1235-3.